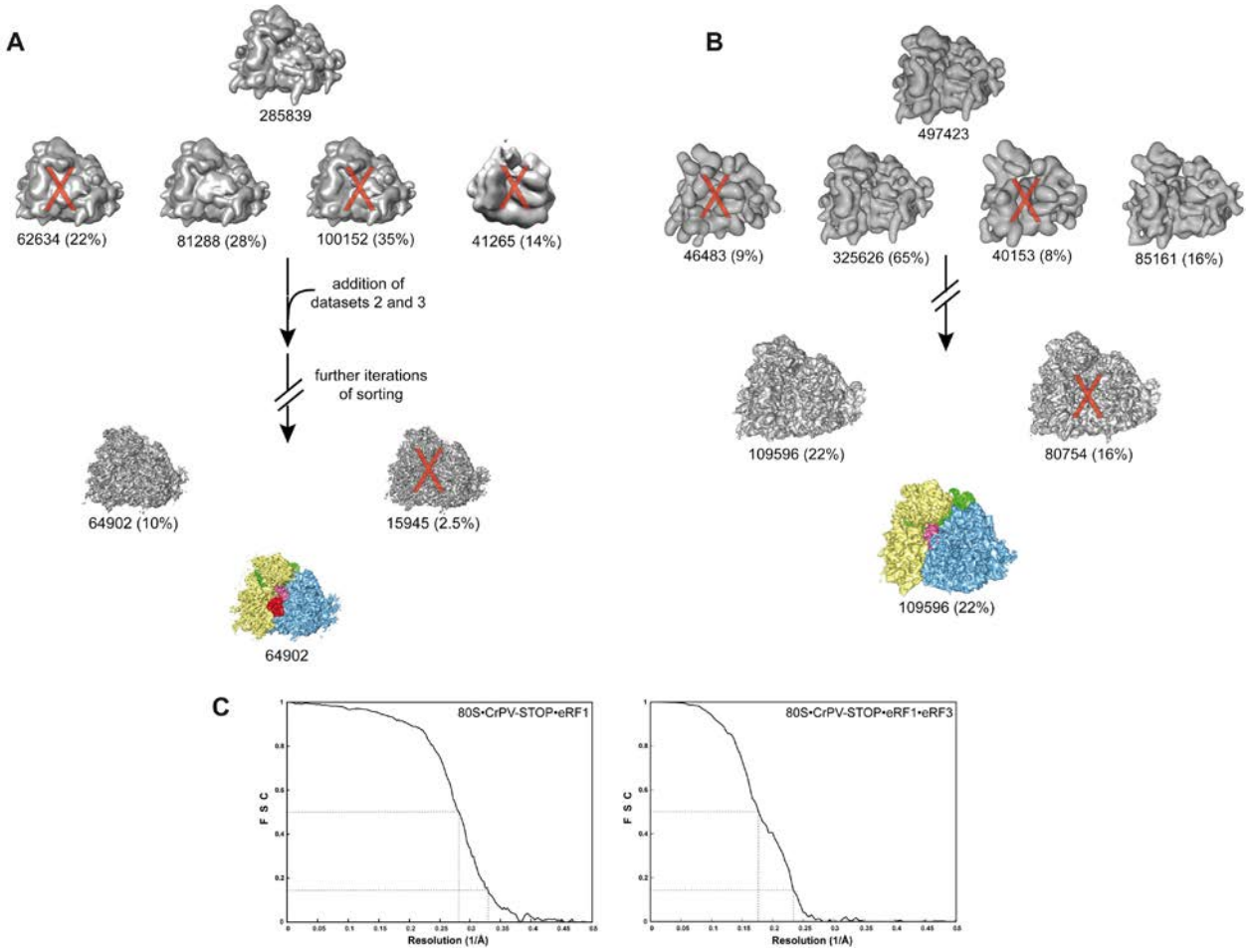

Figure S1. Heterogeneity in the 80S termination complexes and resolution curves, related to Figure 2.

Overview of key points during multireference sorting of termination complexes using SPIDER (Frank et al., 1996). (A) The 80S•CrPV-STOP•eRF1•eRF3•GMPPNP complex was processed from three sub-datasets with a total of ~ 630,000 particle images. Subset 1 contained 285,839 particle images of which 81,288 were used for the combination with subsets 2 and 3. Finally, 64,902 particle images were assigned to the termination complex. (B) Sorting of the 80S•CrPV-STOP•eRF1 dataset was started with 497,423 particle images. After several steps of alignment a total number of 109,596 particle images resembled the desired complex. (C) The Fourier Shell Correlation (FSC) curves of the final reconstructions were calculated semi-independently. Dotted lines indicate the $FSC_{0.5}$ or $FSC_{0.143}$ respectively.

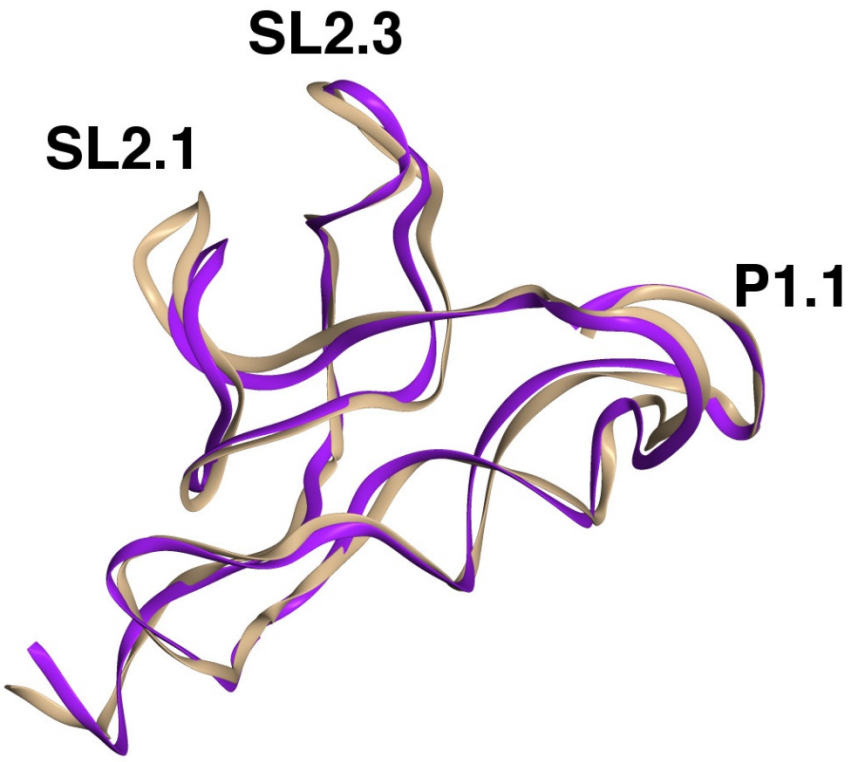

Figure S2. Comparison of the CrPV IRES structure modeled based on the cryo-EM map from Schüler et al. with the structure based on the high resolution cryo-EM map from Fernández et al. ,

related to Figure 3.

Superposition of the ribosome-binding domain from the model by Schüler et al. (Schüler et al., 2006, purple) with the model by Fernández et al. (Fernández et al., 2014, brown). Both models were aligned on each other as rigid bodies and the RMSD value between both models was calculated based on the phosphate atoms of the backbone.

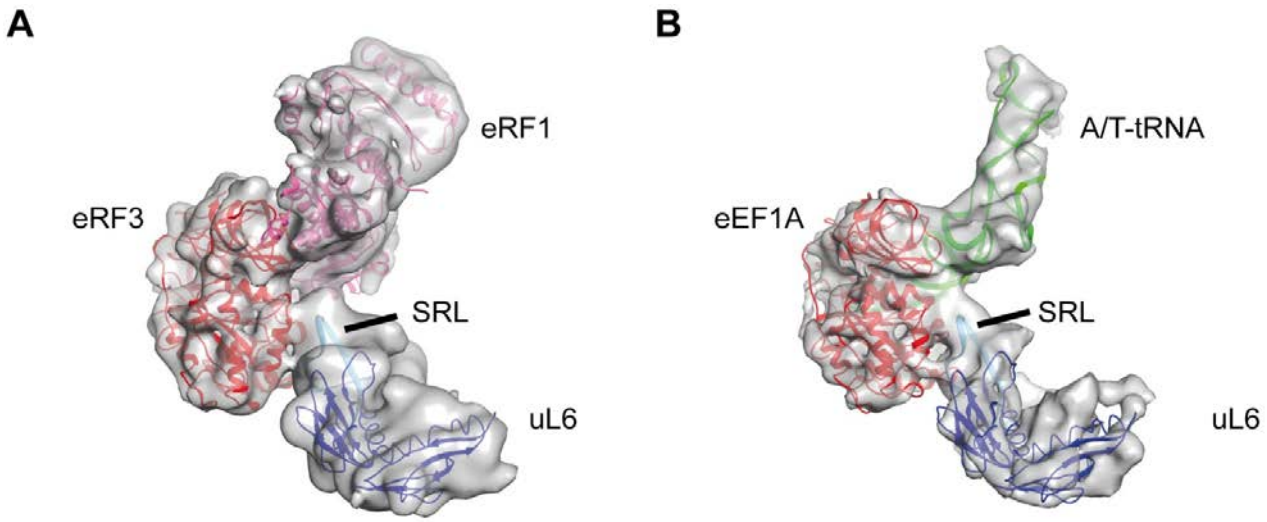

Figure S3. Comparison of the aa-tRNA•eEF1A•GMPPNP complex with the eRF1•eRF3•GMPPPNP complex and the interaction with the SRL, related to Figure 6.

Structural models for (A) eRF1 and eRF3 (this work) as well as (B) eEF1A and an A/T tRNA (Budkevich et al., 2014) were fitted into the corresponding electron density maps. The interaction pattern with the SRL (cyan) differs between the two complexes. In the termination complex (A) the SRL is exclusively bound via eRF3, eRF1 is not involved in the interaction. In contrast, the interaction of eEF1A to the SRL (B) is accompanied by the A/T tRNA.

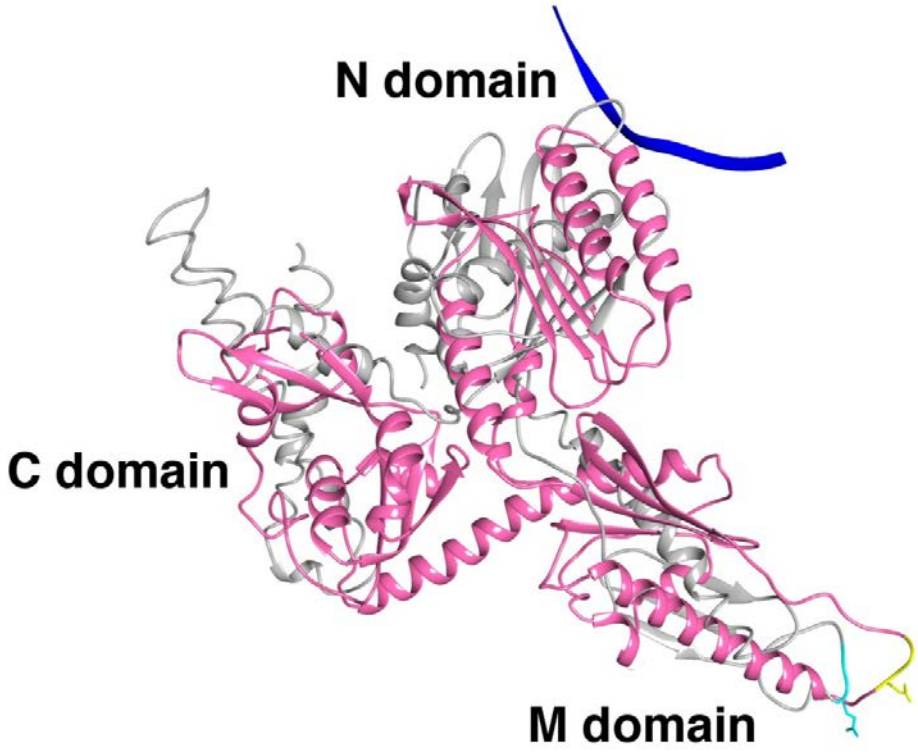

Figure S4. Overlap of the bacterial RF2 structure with eRF1 model, related to Figure 7.

Overlap of the X-Ray structure of bacterial RF2 (Jin et al., 2010, gray, GGQ shown in cyan) with eRF1 model (hot pink, GGQ shown in yellow) from the 80S•CrPV-STOP•eRF1 complex when the corresponding small ribosomal subunits were aligned along their rRNA core. The mRNA is shown in blue.

SUPPLEMENTAL EXPERIMENTAL PROCEDURES

Plasmids

Expression vectors for His_6-tagged human eRF1 and eRF3aC lacking the N-terminal 138 a.a. (referred to as eRF3 throughout the text) have been described (Frolova et al., 1998, 2002). The CrPV-STOP transcription vector was made by inserting a DNA fragment, containing the *wt* CrPV IRES flanked by a T7 promoter and an UAA stop codon, into pUC18. CrPV-STOP mRNA was transcribed using T7 RNA polymerase after linearization of the vector with SspI.

Purification of factors and ribosomal subunits

Native eEF2, and 40S and 60S ribosomal subunits were purified from rabbit reticulocyte lysate as described (Pisarev et al., 2007; Pestova and Hellen, 2003). Recombinant His_6-tagged eRF1 and eRF3 were expressed and purified from *E. coli* (Alkalaeva et al., 2006 and references therein).

Toe-printing analysis of ribosomal complexes

2.8 pmol of CrPV-STOP mRNA were incubated with different combinations of 3 pmol 40S subunits, 4.2 pmol 60S subunits, 6 pmol eEF2, 30 pmol eRF1 alone, and a mixture of 7 pmol eRF1 with 9 pmol eRF3 (as indicated in Fig. 1) in 40 µl buffer containing 20 mM Tris pH 7.5, 100 mM KCl, 1mM DTT, 2.5 mM $MgCl_2$ and supplemented with 0.5 mM GTP or GMPPNP for 10 min at 37 ^{0}C. Assembled ribosomal complexes were analyzed *in situ* by toe-printing using avian myeloblastosis virus reverse transcriptase and a ^{32}P-labelled primer complementary to CrPV-STOP mRNA as described (Pisarev et al. 2007). cDNA products were resolved in 6% polyacrylamide sequencing gels.

Sample preparation

For the 80S•CrPV-STOP•eRF1 complex, 2.8 pmol 40S and 4 pmol 60S were incubated with 3.8 pmol CrPV-STOP mRNA and 5 pmol eEF2 in 40 µl binding buffer containing 20 mM Tris pH 7.5, 100 mM KCl, 1 mM DTT, 2.5 mM $MgCl_2$ and supplemented with 0.5 mM GTP for 15 min at 37^0C. Subsequently, 1 µl 240 mM $MgCl_2$ was added to the mixture and the incubation continued for additional 5 min.

The 80S•CrPV-STOP•eRF1•eRF3 complex was prepared by incubating 14.3 pmol 40S, 19.9 pmol 60S, 19 pmol CrPV-STOP mRNA and 5 pmol eEF2 with 200 µM GTP in binding buffer (Mix A) for 15 min at 37 °C in a total volume of 20 µl. The translocation reaction was stopped by addition of 3 mM GMPPNP. To ensure that Mg^{2+} concentration were identical, we added 3 mM $MgCl_2$ to Mix A (Alkalaeva et al., 2006). Separately 35 pmol eRF1 and 68 pmol eRF3 were incubated in 10 µl binding buffer (Mix B) containing 1 mM GMPPNP for 10 min at 37 °C. Next, Mix A and Mix B were combined and incubated for 15 min at 37 °C. After supplementation with additional 6 mM $MgCl_2$ a final incubation time of 5 min completed the reaction.

Cryo-Electron microscopy and Image processing

A total of 3.5 µl of each sample at a concentration of 30 nM was applied on glow-discharged holey carbon grids (Quantifoil, Germany) and immediately vitrified in liquid ethane using a Vitrobot device (FEI). Images were recorded on film (Kodak SO-163) or fully automated using LEGINON program in combination with the *Tietz TemCam F416* CMOS camera for the 80S•CrPV-STOP•eRF1 and the 80S•CrPV-STOP•eRF1•eRF3•GMPPNP complex, respectively, using an FEI Tecnai G^2 Polara operating at 300 kV. The nominal magnification was 39,000 for the 80S•CrPV-STOP•eRF1 and 115000 for the 80S•CrPV-STOP•eRF1•eRF3•GMPPNP complex, respectively. The film data was digitized on a drum-scanner (Heidelberg) with a pixel

size of 1.26 Å on the object scala, CMOS data was acquired with a pixel size of 0.785 Å. The resulting micrographs were evaluated according to drift, astigmatism and their power spectra and the particles were pre-selected using Signature (Chen and Grigorieff, 2007) followed by automated particle picking algorithms. The selected images were boxed out and subjected to multiparticle refinement (Budkevich et al., 2011; Loerke et al., 2010; Ratje et al., 2010). This and all further image processing steps were performed using SPIDER (Frank et al., 1996), the final structures were reconstructed using SPARX (Hohn et al., 2007).

The initial reconstructions were calculated using 366 micrographs with 497,423 particle images for the 80S•CrPV-STOP•eRF1 complex and 10033 micrographs containing 285839 particle images for the 80S•CrPV-STOP•eRF1•eRF3•GMPPNP complex. Right from the initial reconstruction, an extra density in the intersubunit space, belonging to the CrPV IGR IRES, and additional density at the factor binding site, belonging either to eRF1 or eRF1•eRF3, could be directly seen in both complexes. However, the factor densities appeared only fragmented reflecting the substoichiometric occupancy of the factors and the overall heterogeneity of the samples. Further image processing and multiparticle alignment procedures improved the quality of the maps and especially that of the factors. The final reconstruction of the 80S•CrPV-STOP•eRF1 complex was obtained from 109,596 (22% of the initial data set) particle images. After increase of the 80S•CrPV-STOP•eRF1•eRF3•GMPPNP dataset to 630,000 particles images (26959 micrographs), the final reconstruction contained 64,902 particle images (10%). The resolution of both reconstructions was determined to ~ 9 Å, according to the FSC curve using the 0.5 cutoff criterion (Figure S1,C) and the maps were filtered accordingly. Rather, both datasets revealed a small population with bound eEF2 and a strong fragmented density in the intersubunit space, which can arise either from the IRES or a

contamination with tRNAs. We did not analyze these populations further, since a safe assignment of the fragmented density was not possible. For the 80S•CrPV-STOP•eRF1•eRF3•GMPPNP complex, the dataset contained an additional subpopulation representing the binary 80S•CrPV STOP complex in the PRE state.

Interpretation and Modelling

eRF3 was modelled based on the homology with its archaeal eEF1A ortholog (aEF1α) from the aEF1α/aRF1 complex (Kobayashi, Saito, Ishitani, Ito, & Nureki, 2012 PDB ID:3VMF) with COOT (Emsley and Cowtan, 2004). The resulting model was iteratively energy minimized with CNS (Brünger et al., 1998), evaluated with PHENIX (Adams et al., 2010) and rebuild with COOT.

For the eRF1 model, individual domains of the human factor (Mantsyzov et al., 2010; Song et al., 2000; PDB IDs 2KTV and 1DT9) were docked as rigid-bodies into the cryo-EM maps using Chimera (Pettersen et al., 2004) followed by flexible fitting procedures using MDfit (Whitford et al., 2011). Final energy minimization was made with CNS. The CrPV-STOP IRES has been modelled based on the previously published X-ray structure for domain 3 (Zhu et al., 2011; PDB ID 3PYS) and cryo-EM model for domains 1 and 2 (Schüler et al., 2006; PDB ID 2NOQ). While the domain 3 structure fitted into our density without any adjustments, domain 1 and 2 were flexible docked using MDFit (Whitford et al., 2011). The initial IRES model was subsequently subjected to several rounds of manual refinement using COOT (Emsley et al., 2010) followed by energy minimization with ERRASER (Chou et al., 2013).

Cryo-EM densities and the atomic models were visualized using Chimera (Pettersen et al., 2004), which was also used to create all images.

SUPPLEMENTAL REFERENCES

Adams, P.D., Afonine, P. V, Bunkóczi, G., Chen, V.B., Davis, I.W., Echols, N., Headd, J.J., Hung, L.-W., Kapral, G.J., Grosse-Kunstleve, R.W., et al. (2010). PHENIX: a comprehensive Python-based system for macromolecular structure solution. Acta Crystallogr. D. Biol. Crystallogr. *66*, 213–221.

Alkalaeva, E.Z., Pisarev, A. V, Frolova, L.Y., Kisselev, L.L., and Pestova, T. V (2006). In Vitro Reconstitution of Eukaryotic Translation Reveals Cooperativity between Release Factors eRF1 and eRF3. 1125–1136.

Brünger, A.T., Adams, P.D., Clore, G.M., DeLano, W.L., Gros, P., Grosse-Kunstleve, R.W., Jiang, J.S., Kuszewski, J., Nilges, M., Pannu, N.S., et al. (1998). Crystallography & NMR system: A new software suite for macromolecular structure determination. Acta Crystallogr. D. Biol. Crystallogr. *54*, 905–921.

Budkevich, T., Giesebrecht, J., Altman, R.B., Munro, J.B., Mielke, T., Nierhaus, K.H., Blanchard, S.C., and Spahn, C.M.T. (2011). Structure and dynamics of the mammalian ribosomal pretranslocation complex. Mol. Cell *44*, 214–224.

Budkevich, T.V., Giesebrecht, J., Behrmann, E., Loerke, J., Ramrath, D.J.F., Mielke, T., Ismer, J., Hildebrand, P.W., Tung, C.-S., Nierhaus, K.H., et al. (2014). Regulation of the Mammalian Elongation Cycle by Subunit Rolling: A Eukaryotic-Specific Ribosome Rearrangement. Cell *158*, 121–131.

Chen, J.Z., and Grigorieff, N. (2007). SIGNATURE: A single-particle selection system for molecular electron microscopy. J. Struct. Biol. *157*, 168–173.

Chou, F.-C., Sripakdeevong, P., Dibrov, S.M., Hermann, T., and Das, R. (2013). Correcting pervasive errors in RNA crystallography through enumerative structure prediction. Nat. Methods *10*, 74–76.

Emsley, P., and Cowtan, K. (2004). Coot: model-building tools for molecular graphics. Acta Crystallogr. D. Biol. Crystallogr. *60*, 2126–2132.

Emsley, P., Lohkamp, B., Scott, W.G., and Cowtan, K. (2010). Features and development of Coot. Acta Crystallogr. Sect. D Biol. Crystallogr. *66*, 486–501.

Fernández, I.S., Bai, X.-C., Murshudov, G., Scheres, S.H.W., and Ramakrishnan, V. (2014). Initiation of Translation by Cricket Paralysis Virus IRES Requires Its Translocation in the Ribosome. Cell *157*, 823–831.

Frank, J., Radermacher, M., Penczek, P., Zhu, J., Li, Y., Ladjadj, M., and Leith, A. (1996). SPIDER and WEB: processing and visualization of images in 3D electron microscopy and related fields. J. Struct. Biol. *116*, 190–199.

Hohn, M., Tang, G., Goodyear, G., Baldwin, P.R., Huang, Z., Penczek, P.A., Yang, C., Glaeser, R.M., Adams, P.D., and Ludtke, S.J. (2007). SPARX, a new environment for Cryo-EM image processing. J. Struct. Biol. *157*, 47–55.

Jin, H., Kelley, A.C., Loakes, D., and Ramakrishnan, V. (2010). Structure of the 70S ribosome bound to release factor 2 and a substrate analog provides insights into catalysis of peptide release. Proc. Natl. Acad. Sci. U. S. A. *107*, 8593–8598.

Kobayashi, K., Saito, K., Ishitani, R., Ito, K., and Nureki, O. (2012). Structural basis for translation termination by archaeal RF1 and GTP-bound EF1α complex. Nucleic Acids Res. *40*, 9319–9328.

Loerke, J., Giesebrecht, J., and Spahn, C.M.T. (2010). Multiparticle cryo-EM of ribosomes. Methods Enzymol. *483*, 161–177.

Mantsyzov, A.B., Ivanova, E. V, Birdsall, B., Alkalaeva, E.Z., Kryuchkova, P.N., Kelly, G., Frolova, L.Y., and Polshakov, V.I. (2010). NMR solution structure and function of the C-terminal domain of eukaryotic class 1 polypeptide chain release factor. FEBS J. *277*, 2611–2627.

Pettersen, E.F., Goddard, T.D., Huang, C.C., Couch, G.S., Greenblatt, D.M., Meng, E.C., and Ferrin, T.E. (2004). UCSF Chimera - A visualization system for exploratory research and analysis. J. Comput. Chem. *25*, 1605–1612.

Ratje, A.H., Loerke, J., Mikolajka, A., Brünner, M., Hildebrand, P.W., Starosta, A.L., Dönhöfer, A., Connell, S.R., Fucini, P., Mielke, T., et al. (2010). Head swivel on the ribosome facilitates translocation by means of intra-subunit tRNA hybrid sites. Nature *468*, 713–716.

Schüler, M., Connell, S.R., Lescoute, A., Giesebrecht, J., Dabrowski, M., Schroeer, B., Mielke, T., Penczek, P.A., Westhof, E., and Spahn, C.M.T. (2006). Structure of the ribosome-bound cricket paralysis virus IRES RNA. Nat. Struct. Mol. Biol. *13*, 1092–1096.

Song, H., Mugnier, P., Das, A.K., Webb, H.M., Evans, D.R., Tuite, M.F., Hemmings, B.A., Barford, D., and Miescher-institut, F. (2000). The Crystal Structure of Human Eukaryotic Release Factor eRF1 — Mechanism of Stop Codon Recognition and Peptidyl-tRNA Hydrolysis. *100*, 311–321.

Whitford, P.C., Ahmed, A., Yu, Y., Hennelly, S.P., Tama, F., Spahn, C.M.T., Onuchic, J.N., and Sanbonmatsu, K.Y. (2011). Excited states of ribosome translocation revealed through integrative molecular modeling. Proc. Natl. Acad. Sci. *108*, 18943–18948.

Zhu, J., Korostelev, A., Costantino, D.A., Donohue, J.P., Noller, H.F., and Kieft, J.S. (2011). Crystal structures of complexes containing domains from two viral internal ribosome entry site (IRES) RNAs bound to the 70S ribosome. Proc. Natl. Acad. Sci. U. S. A. *108*, 1839–1844.